The Strength of the Brewer–Dobson Circulation in a Changing Climate: Coupled Chemistry–Climate Model Simulations

Feng Li

Atmospheric and Oceanic Sciences Program, Princeton University, Princeton, New Jersey

John Austin and John Wilson

NOAA/Geophysical Fluid Dynamics Laboratory, Princeton, New Jersey

ABSTRACT

The strength of the Brewer–Dobson circulation (BDC) in a changing climate is studied using multidecadal simulations covering the 1960–2100 period with a coupled chemistry–climate model, to examine the seasonality of the change of the BDC. The model simulates an intensification of the BDC in both the past (1960–2004) and future (2005–2100) climate, but the seasonal cycle is different. In the past climate simulation, nearly half of the tropical upward mass flux increase occurs in December–February, whereas in the future climate simulation the enhancement of the BDC is uniformly distributed in each of the four seasons. A downward control analysis implies that this different seasonality is caused mainly by the behavior of the Southern Hemisphere planetary wave forcing, which exhibits a very different long-term trend during solstice seasons in the past and future. The Southern Hemisphere summer planetary wave activity is investigated in detail, and its evolution is found to be closely related to ozone depletion and recovery. In the model results for the past, about 60% of the lower-stratospheric mass flux increase is caused by ozone depletion, but because of model ozone trend biases, the atmospheric effect was likely smaller than this. The remaining fraction of the mass flux increase is attributed primarily to greenhouse gas increase. The downward control analysis also reveals that orographic gravity waves contribute significantly to the increase of downward mass flux in the Northern Hemisphere winter lower stratosphere.

1. Introduction

The Brewer–Dobson circulation (BDC), also known as the stratospheric meridional residual circulation, is driven by extratropical wave forcing in the middle atmosphere (Holton 1995). It consists of an upward motion across the tropopause in the Tropics and downward return flows in the extratropics in each hemisphere. Recent climate model studies have found that the BDC will intensify with the increase of greenhouse gases (GHGs; e.g., Rind et al. 1998; Butchart and Scaife 2001; Sigmond et al. 2004; Butchart et al. 2006). It is recognized that the intensification of the BDC is caused primarily by enhancement of the extratropical planetary wave forcing in the middle atmosphere via the "downward control" principle (Haynes et al. 1991).

GHG increase causes troposphere warming and stratosphere cooling, leading to an enhanced meridional temperature gradient in the upper troposphere and lower stratosphere (UTLS). It has been argued that the increased meridional temperature gradient results in enhanced planetary wave activity in the troposphere, and increased planetary wave propagation into the stratosphere (Rind et al. 1998; Sigmond et al. 2004; Eichelberger and Hartmann 2005). Note that Sigmond et al. (2004) found that parameterized gravity waves are important in driving an increased BDC in their double-CO_2 experiments. Butchart et al. (2006) also noted that subgrid-scale waves make a nonnegligible contribution to the intensification of the BDC.

By cooling the polar lower stratosphere, ozone depletion can also increase the latitudinal temperature gradient in the UTLS region, hence enhancing the BDC in the same fashion as GHG increases. The long time record of radiosonde and satellite data have revealed that, coinciding with the observed ozone loss,

_____

Corresponding author address: Feng Li, NASA GSFC, Code 613.3, Greenbelt, MD 20771.
E-mail: fengli@welkin.gsfc.nasa.gov

the Antarctic lower stratosphere exhibited a significant cooling trend in spring during the last two decades (Randel and Wu 1999). This cooling is coupled with an upper-stratospheric warming, which is attributed to increased adiabatic heating. A number of general circulation model (GCM) simulations have produced similar results (Mahlman et al. 1994; Shindell et al. 1997; Graf et al. 1998; Austin and Butchart 2003). It should be emphasized that this phenomenon is a strong seasonal feature, because the cooling is strongest in the Southern Hemisphere (SH) springtime and is smaller, but still significant, in the summer, while no systematic change is observed in the winter (Randel and Wu 1999).

It is clear that both the effects of the GHG increase and ozone depletion should be included in order to understand the evolution of the BDC better. The purpose of this study is to investigate the strength of the BDC in a changing climate using the Geophysical Fluid Dynamics Laboratory (GFDL) coupled chemistry–climate model. We will focus on the seasonal behavior of the long-term trend of the BDC, how ozone depletion and its recovery affect the strength of the BDC, and the underlying mechanism responsible for the changes.

2. Model and simulations

Details of the new GFDL coupled chemistry–climate model, the Atmospheric Model with Transport and Chemistry (AMTRAC), are described in Austin et al. (2007) and Austin and Wilson (2006). The model is an extension of the GFDL Atmospheric Model version 2 (AM2; GFDL Global Atmospheric Model Development Team 2004). AMTRAC has 48 levels with the top at 0.002 hPa. The horizontal resolution is 2° latitude by 2.5° longitude. All of the physical and radiative processes are parameterized in the same way as that of the GFDL Global Atmospheric Model Development Team (2004), except that the Alexander and Dunkerton (1999) scheme is implemented to parameterize nonorographic gravity wave forcing in the middle atmosphere. The chemistry module is a comprehensive stratospheric scheme with simplified tropospheric chemistry.

Two 30-yr control runs with fixed concentrations of GHGs, chlorofluorocarbons (CFCs), and aerosols for 1960 (TS1960) and 2000 (TS2000) were first completed. Ensemble transit simulations with three members of the past (1960–2004) and future (1990–2100) were then performed. The three past runs were initialized from year 10, 20, and 30 of the TS1960 run, and the future runs were initialized from 1 January 1990 of the corresponding past runs. For the past runs, the model was forced with observed time-dependent sea surface tem-

perature and sea ice amounts, concentration of GHGs, CFCs, and aerosols. The observed solar cycle was included by specifying the radiative fluxes at the top of the atmosphere. For the future runs, sea surface temperature and sea ice amounts were taken from the GFDL coupled atmosphere–ocean model simulation [simulation Climate Model version 2.1 (CM 2.1) of Delworth et al. (2006)]. The Intergovernmental Panel on Climate Change (IPCC) scenario A1B (Houghton et al. 2001) was used for the GHGs. CFCs were taken from the World Meteorological Organization (WMO 2002, chapter 1, reference profile A1).

Ensemble mean results will be presented in this study. There is a 15-yr overlap in the 1990–2004 period between the past and future runs, and the future run results will be discussed only for the 2005–2100 period. An additional simulation (Cly1960) was completed for the period of 1960–2004 with fixed 1960 levels of halogen concentrations, but with all other forcings the same as in the past transit run. The results of this simulation were used to try to separate the impact of ozone depletion versus GHG change.

3. Evolution of the Brewer–Dobson circulation in the past climate simulation

The strength of the BDC can be characterized by the magnitude of the upward mass flux into the lower tropical stratosphere. The tropical upwelling is confined between the so-called turnaround latitudes, where the residual vertical velocity changes sign (Rosenlof 1995). Figure 1 shows the evolution of the tropical upward mass flux in the lower and middle stratosphere from 1960 to 2004. The upward mass flux had large multiannual variations, but overall it increased throughout the lower and middle stratosphere. The secular change of the mass flux was not uniform, though. For example, at 77 hPa, the overall trend was $2.7 \pm 0.3 \, (1\sigma)\%$ decade^{-1}, but the upward mass flux did not show a systematic change during the 1960–74 period with a trend of $-0.3 \pm 1.3\%$ decade^{-1}, and it increased rapidly in the 1975–99 period with a trend of $4.3 \pm 0.75\%$ decade^{-1}. At higher levels, the increase of the upwelling occurred mainly in the period from middle 1970s to early 1990s. All ensemble members show similar results, suggesting that these changes were caused by external forcing. The results suggest that the increase of the BDC after the mid-1970s was largely driven by ozone depletion (section 8).

As mentioned in the introduction, it is expected that the intensification of the BDC would show strong seasonality if cooling of the Antarctic lower stratosphere resulting from ozone depletion plays an important role.
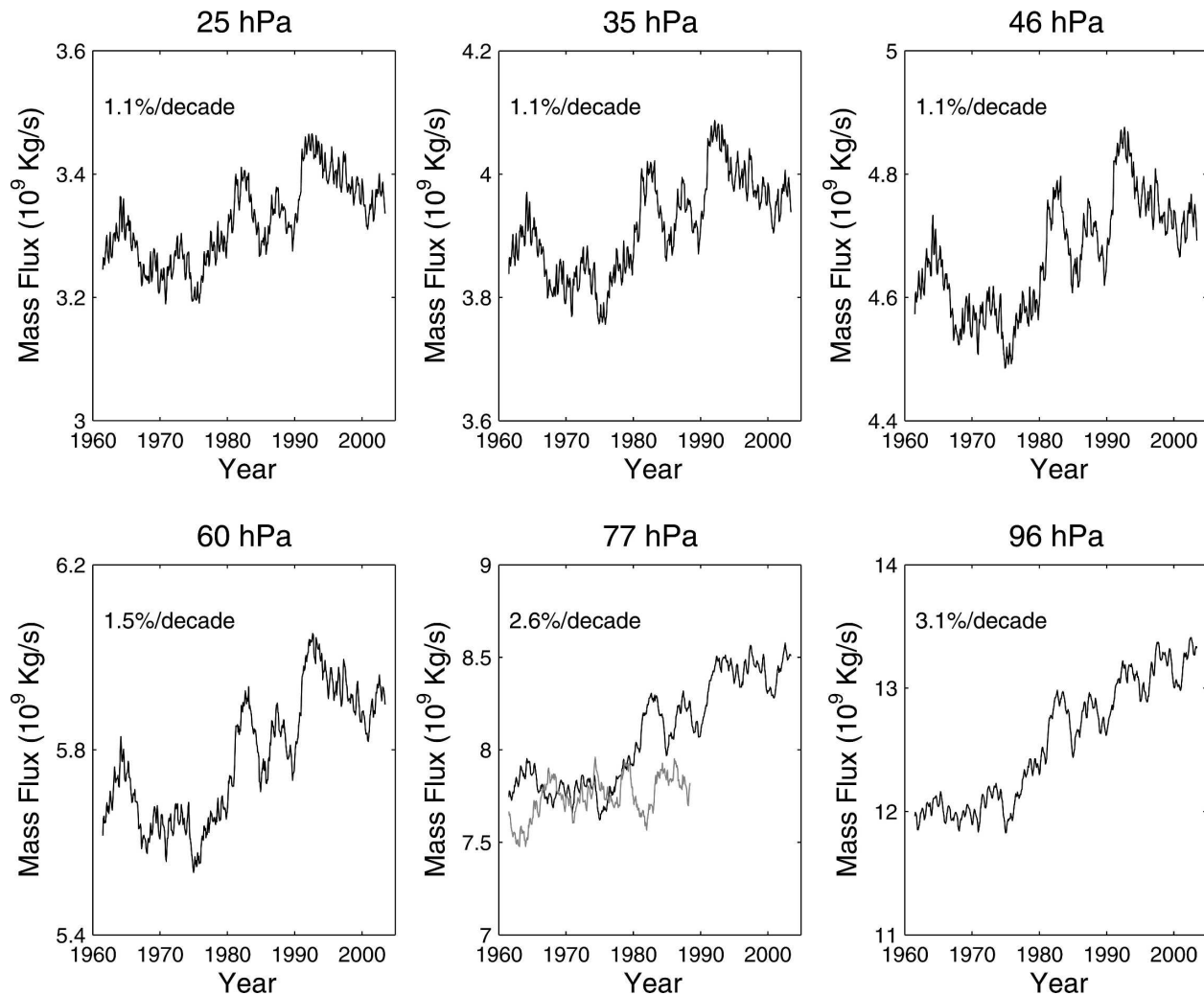
FIG. 1. Evolution of the monthly mean (37-month running average) tropical upward mass flux in the January 1960–December 2004 period in six model levels in the lower and middle stratosphere for the past climate runs. The linear trend (derived from annual mean upward mass flux) is indicated at the top of each panel. Results from TS1960 are also plotted at 77 hPa (gray line).

Figure 2 shows the seasonal mean mass flux at 77 hPa. Note that the tropical upward mass flux balances the net Northern Hemisphere (NH) and SH downward mass flux. Figures 2a–c show that the seasonal cycle in the NH downward mass flux is out of phase and is stronger than that in the SH downward mass flux. As a result, the seasonal cycle in the tropical upwelling is driven by the NH seasonal cycle. However, the change in the tropical upward mass flux behaves differently.

To see the seasonal nature of the change of the mass flux more clearly, the mean for each season has been subtracted from the mass flux at 77 hPa and the results are plotted in Figs. 2d–f. The evolution of the tropical upward mass flux is different for each season. For example, in June–August (JJA) the upward mass flux stopped increasing in the middle 1980s, but in December–February (DJF) the mass flux continued to increase until the early 2000s.

Figure 2d clearly shows that the increase of the tropical upward mass flux is not uniformly distributed seasonally, with DJF contributing the largest portion. Among the increase of 9.14×10^8 kg s^{-1} in the annual mean mass flux during the 1960–2004 period, DJF, March–May (MAM), JJA, and September–November (SON) accounted for 40%, 26%, 16%, and 18%, respectively (also see Fig. 6). Examining the behavior of the NH and SH downward mass flux reveals that the SH played an essential role in determining this strong seasonal feature. In the NH, all seasons exhibited similar temporal changes except in JJA when the increase of the mass flux was weak (Fig. 2e). In the SH, however, the evolution in the four seasons is quite different
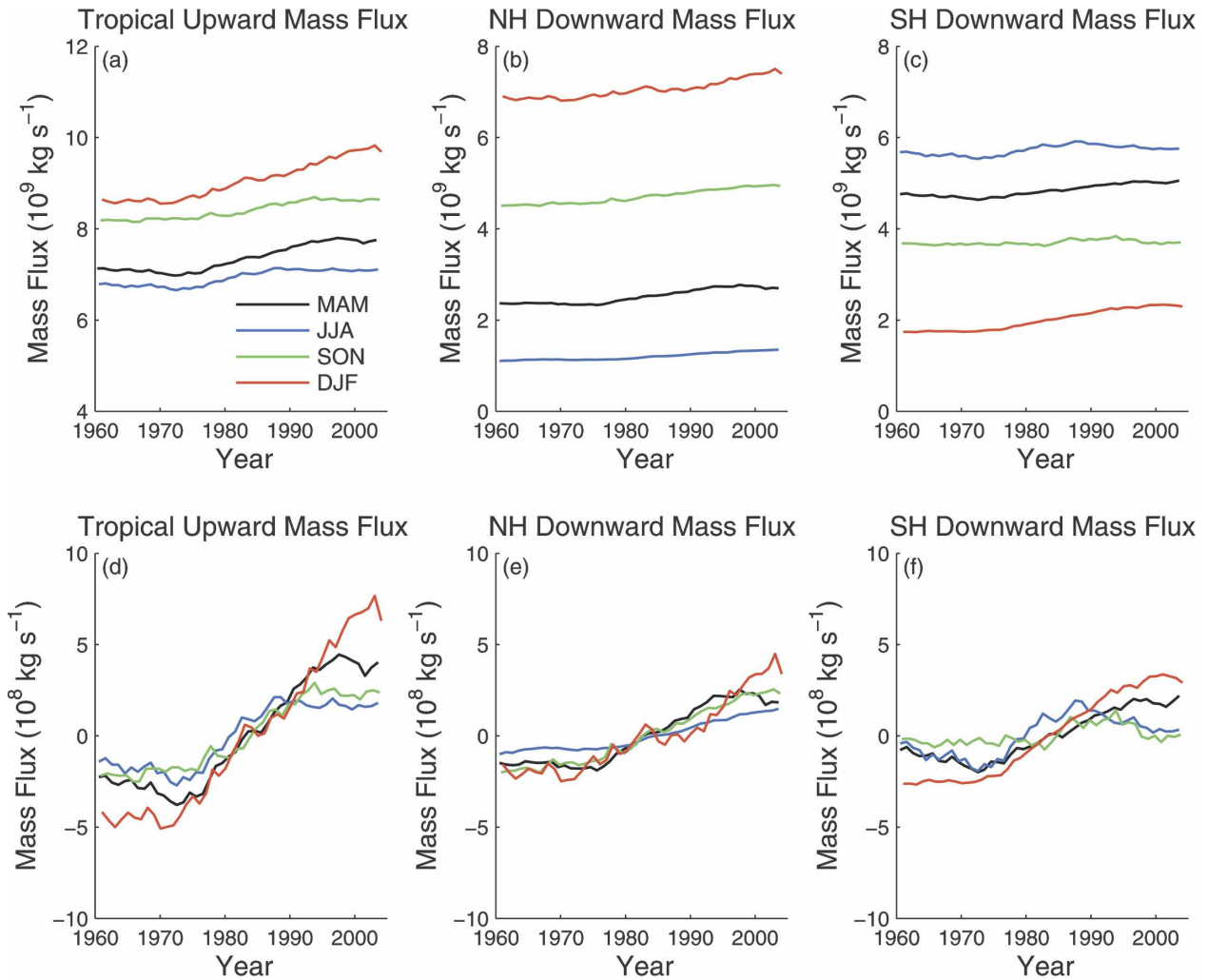
FIG. 2. Seasonal distribution of the mass flux at 77 hPa for the past runs. (a) Integrated tropical upward mass flux between the turnaround latitudes. (b) Integrated NH downward mass flux between the North Pole and the NH turnaround latitude. (c) Integrated SH downward mass flux between the South Pole and the SH turnaround latitude. (d)–(f) Same as in (a)–(c), but the mean is subtracted. Note that the scale is different between the top and bottom panels.

(Fig. 2f). It appears that the seasonal cycle of the tropical mass flux trend is largely determined by the SH seasonal cycle. The reason that the largest increase of the tropical upward mass flux occurred in DJF is because the SH contributed a significant amount (about 55%) to the DJF mass flux increase. That is to say, in DJF, although the NH net downward mass flux was more than 3 times larger than the SH counterpart (Figs. 2b,c), the SH actually balanced more of the tropical upward mass flux increase.

The spatial structure of the changes in the BDC is illustrated in Fig. 3, which shows the changes in the residual vertical velocity ($\overline{\omega}^*$) as a function of latitude and pressure for the four seasons. The blue-shaded region indicates stronger upward (weaker downward) motion, while the yellow and red regions indicate stronger downward (weaker upward) motion. The tropical upwelling was intensified in the lower stratosphere in all seasons, consistent with the tropical upward mass flux evolution shown in Fig. 1. In fact, Fig. 3 shows that the enhancement of the tropical upwelling extended to the upper stratosphere. In the lower stratosphere, the large increase of the tropical upwelling was primarily balanced by enhanced downwelling in the midlatitude region.

Substantial changes were also found in the polar stratosphere. The change of the BDC in the polar stratosphere was season and hemisphere dependent. In the Antarctic lower stratosphere, the downward motion was significantly enhanced in DJF, whereas it was slightly reduced in JJA. In SON, a weakening of the
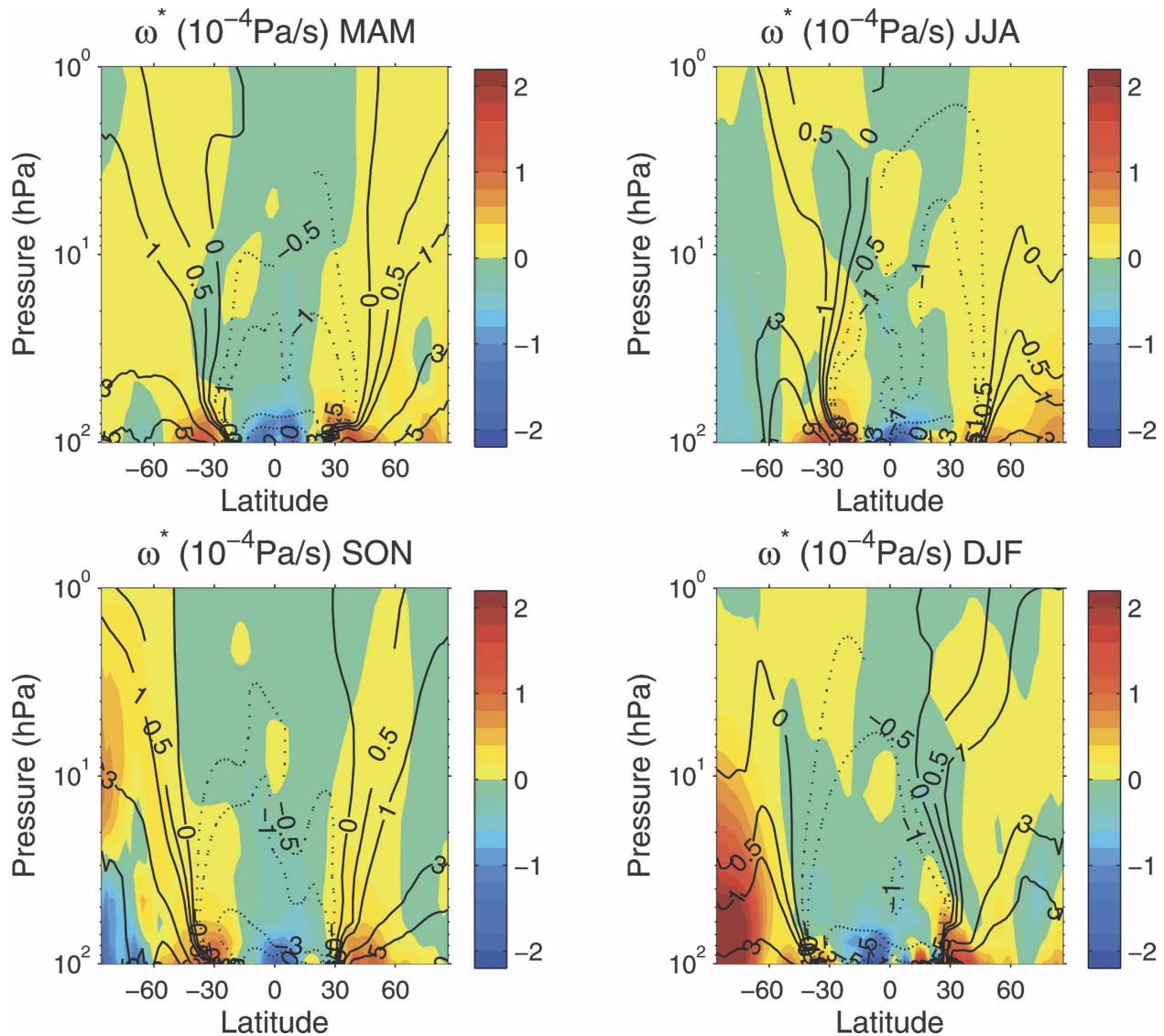
FIG. 3. Changes of the residual vertical velocity for each season as a function of latitude and pressure. The contours are the mean of the first 10-yr simulations (1960–69) and the shades are the changes during the 1960–2004 period. The black solid (dashed) lines indicate downward (upward) motion. Contour intervals are −5, −3, −1, −0.5, 0, 0.5, 1, 3, 5. The bluish regions denote enhanced upwelling (or reduced downwelling) and the yellow/red regions indicate enhanced downwelling (or reduced upwelling).

downward motion in the lower stratosphere was accompanied by an enhancement in the upper stratosphere. Downwelling in the Arctic lower stratosphere was largely increased in MAM and JJA, but it was less significant and the structure was more complex in SON and DJF.

4. Evolution of the Brewer–Dobson circulation in the future climate simulation

The future transit runs also yielded an increase of the tropical upward mass flux in the lower stratosphere (Fig. 4). Similar to the past transit simulations, the tropical upward mass flux exhibited large multiannual variations, but the overall long-term upward trend is evident. However, the increase of the mass flux in the lower stratosphere was reduced in the future climate. The trends at 77 and 96 hPa in the future runs were much smaller compared to those in the past runs. At higher levels, the trends were similar in the past and future runs. For comparison, the mass flux at 77 hPa from the control simulation with fixed concentrations of GHGs, CFCs, and aerosols at 2000 (TS2000) is also plotted in Fig. 4. In contrast to the future runs, the TS2000 mass flux did not show a trend, indicating that the trend was caused by external forcing factors.
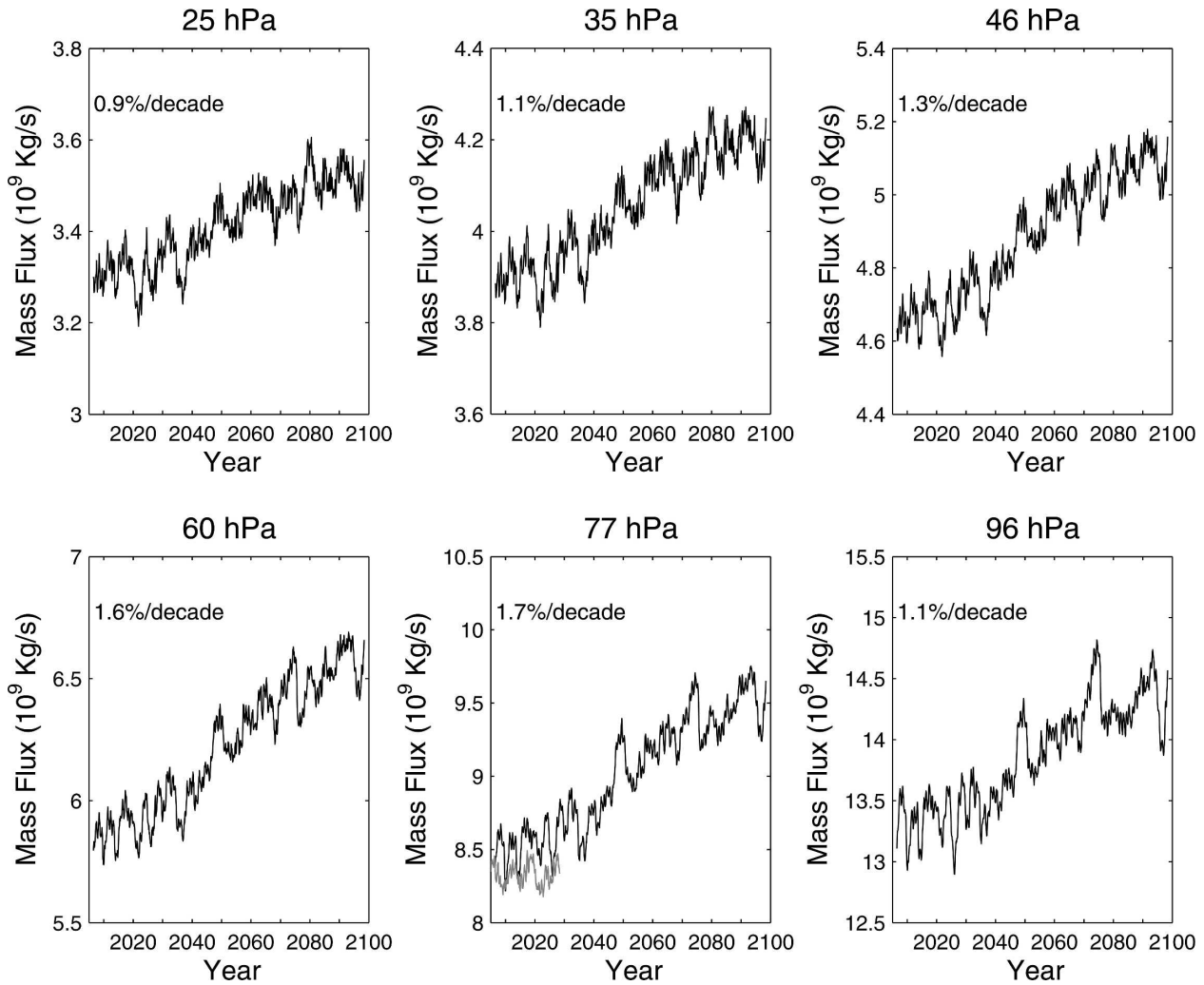
FIG. 4. Same as in Fig. 1, but for the future runs for the January 2005–December 2099 period. The gray line at 77 hPa is the result from TS2000.

Figures 5a–c show that the seasonal cycle of the tropical upwelling at 77 hPa was driven by the seasonal cycle of the NH downwelling with the largest upward mass flux found in DJF and the smallest in JJA, which is similar to the past run results. However, the seasonal cycle of the tropical upward mass flux trend is different from that in the past runs. Figure 5d shows that all four seasons had similar long-term changes in the 2005–2100 period, with each season contributing nearly equally to the increase of 1.29×10^9 kg s^{-1} in the annual mean tropical upward mass flux at 77 hPa. In each hemisphere, the largest increase occurred in the winter season (Figs. 5e,f).

Figure 6 summarizes the seasonal cycle of the mass flux and mass flux trend at 77 hPa. In the past and future climate simulations, the seasonal cycle of the mass flux did not change, but the seasonal cycle of the

tropical upward mass flux trend was very different. The different seasonality of the tropical upwelling trend between the past and future climate simulations was primarily driven by the different seasonal cycle of the SH downward mass flux trend in the past and future, especially in the DJF and JJA seasons. In the past runs, DJF accounted for half of the SH mass flux increase, while only 18% of the mass flux increase occurred in JJA. A near-opposite case was found in the future runs: there was no significant SH downward mass flux change in DJF and 45% of the SH downward mass flux increase happened in JJA.

5. Mechanisms for the intensification of the Brewer–Dobson circulation

The mechanisms responsible for the strengthening of the BDC are investigated using the downward control
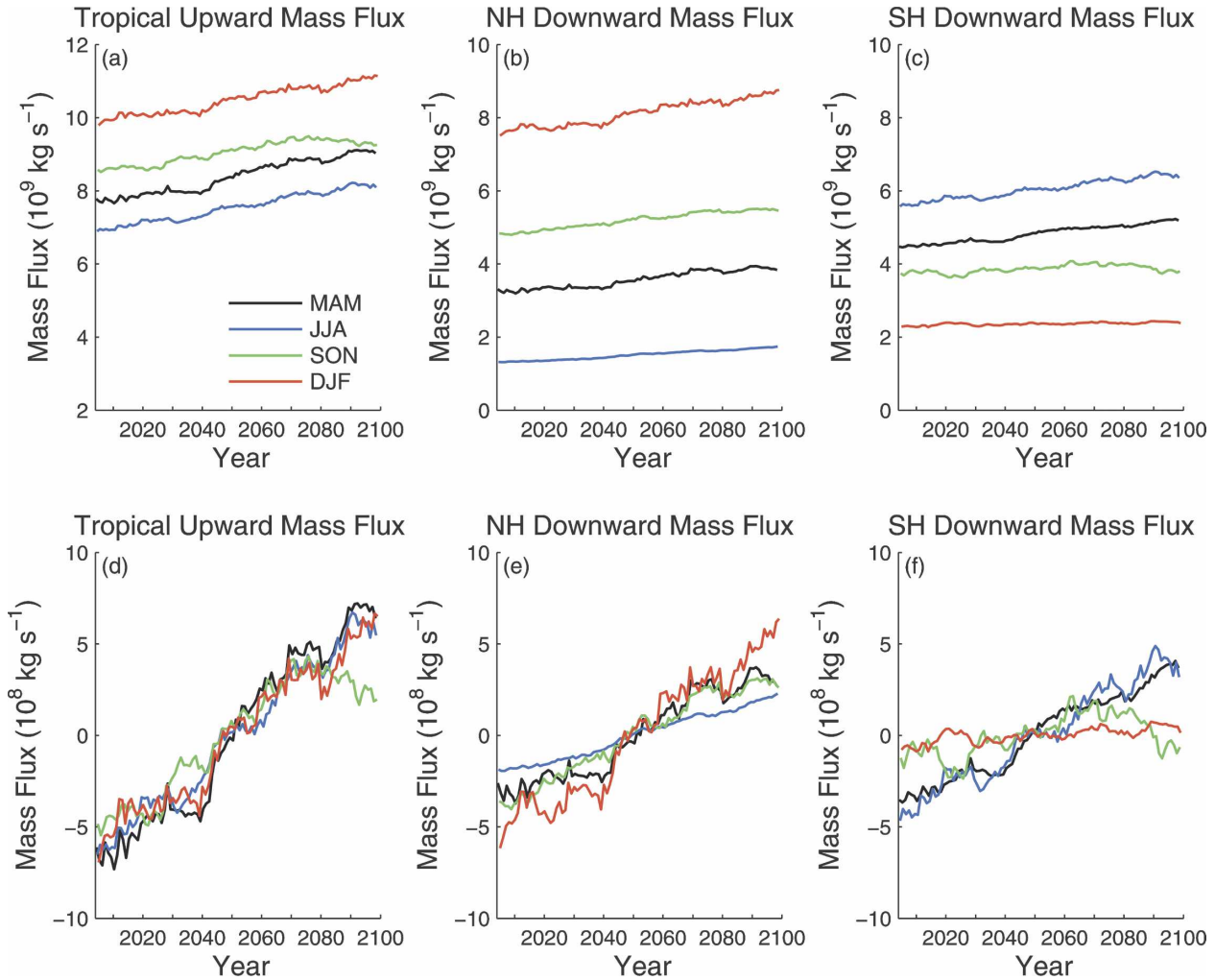
FIG. 5. Same as in Fig. 2, but for the future runs.

principle. Assuming steady state, Haynes et al. (1991) showed that the residual streamfunction can be expressed as

$$\psi(\phi, z) = \int_z^\infty \left(\frac{\rho_0 a^2 \mathcal{F} \cos^2\phi}{\overline{m}_\phi} \right)_{\phi=\phi(z')} dz', \qquad (1)$$

where ϕ is the latitude, z is the log pressure height, ρ_0 is the density, a is the radius of the earth, F is the total wave forcing, $\overline{m} = a \cos\phi(\overline{u} + a\Omega \cos\phi)$ is the zonal mean angular momentum, $\overline{u}$ is the zonal mean zonal wind, Ω is the angular velocity of the earth, the subscript denotes derivative, and the integral is along a contour $\phi(z)$ of constant angular momentum. The total wave forcing F in the model consists of the Eliassen–Palm flux divergence (EPFD) resulting from resolved planetary waves, and parameterized orographic gravity wave drag (OGWD) and nonorographic gravity wave

drag. In the lower stratosphere, EPFD and OGWD are the most important wave forcings. By calculating the streamfunction using (1) with EPFD and OGWD, we can obtain insight into how planetary waves and orographic gravity waves contribute to the intensification and the seasonal cycle of the BDC.

The steady-state assumption is approximately satisfied under seasonal mean conditions (Newman et al. 2001). Figure 7 compares the SH and NH downward mass flux at 77 hPa in JJA and DJF calculated using the downward control principle. The hemispheric mass flux contributions for planetary waves and orographic gravity waves are calculated at the turnaround latitude determined from the residual streamfunction. Figure 7 shows that the mass flux resulting from total wave forcing (EPFD + OGWD) agrees quite well with the residual mass flux, indicating that the downward control method is valid.
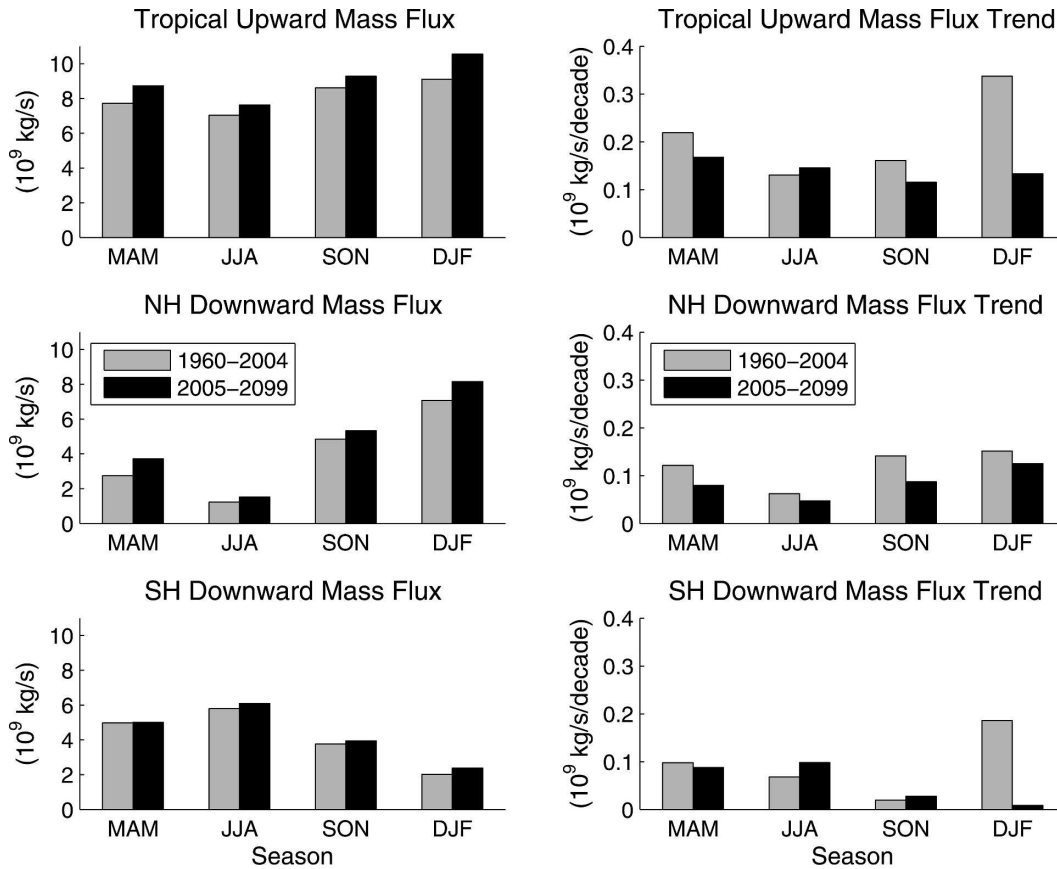
FIG. 6. (left) Seasonal cycle of the mass flux (right) and the mass flux trend at 77 hPa.

Planetary waves and orographic gravity waves played very different roles in driving the change of the BDC in the NH and SH. In the SH, the long-term trend in the downward mass flux and its seasonal cycle were almost solely determined by planetary waves, with orographic gravity waves having only a minor effect on the change of the SH mass flux. Almost the opposite situation was found in the NH. The intensification of the NH downward mass flux occurred mainly in winter, which is attributed to the increase of the orographic gravity wave forcing.

We have shown in section 4 that the difference in the seasonality of the tropical upward mass flux trends between the past and future simulations was caused primarily by the differing evolution of the SH downward mass flux during the solstice seasons. Because the change of the SH downwelling was mainly driven by planetary waves, it is concluded that the SH planetary wave forcing caused these differences in the seasonal cycle of the BDC trends. In JJA, a small downward trend in the SH planetary wave forcing in the past decades became a large upward trend in the future (Figs. 7a,e). In DJF, SH downward mass flux resulting from

planetary wave forcing underwent a large increase in the period between the middle 1970s and the late 1990s (Fig. 7b), while it did not show a long-term trend in the future (Fig. 7f).

In AMTRAC, the orographic gravity wave drag peaks in the UTLS region and decreases rapidly with height (section 9). Figure 8 shows the downward control analysis at 46 hPa. At this level, the contribution resulting from orographic gravity waves is negligible. As a result, the changes of both the NH and SH downward mass flux are almost entirely determined by planetary wave activity. The behavior of the SH planetary wave forcing at 46 hPa was similar to that at 77 hPa, with opposite long-term trends in the past and future runs (Figs. 8a,b,e,f). The evolution of the planetary wave activity in the NH winter in the future simulation was quite different at 46 and 77 hPa (Figs. 7h and 8h). At 46 hPa, an increase in the planetary wave forcing caused the strengthening of the NH winter downward mass flux (Fig. 8h), whereas at 77 hPa the planetary wave forcing did not show a long-term trend in the NH winter (Fig. 7h). Interestingly, the mass flux increased at both levels, but the driving force changed from pri-
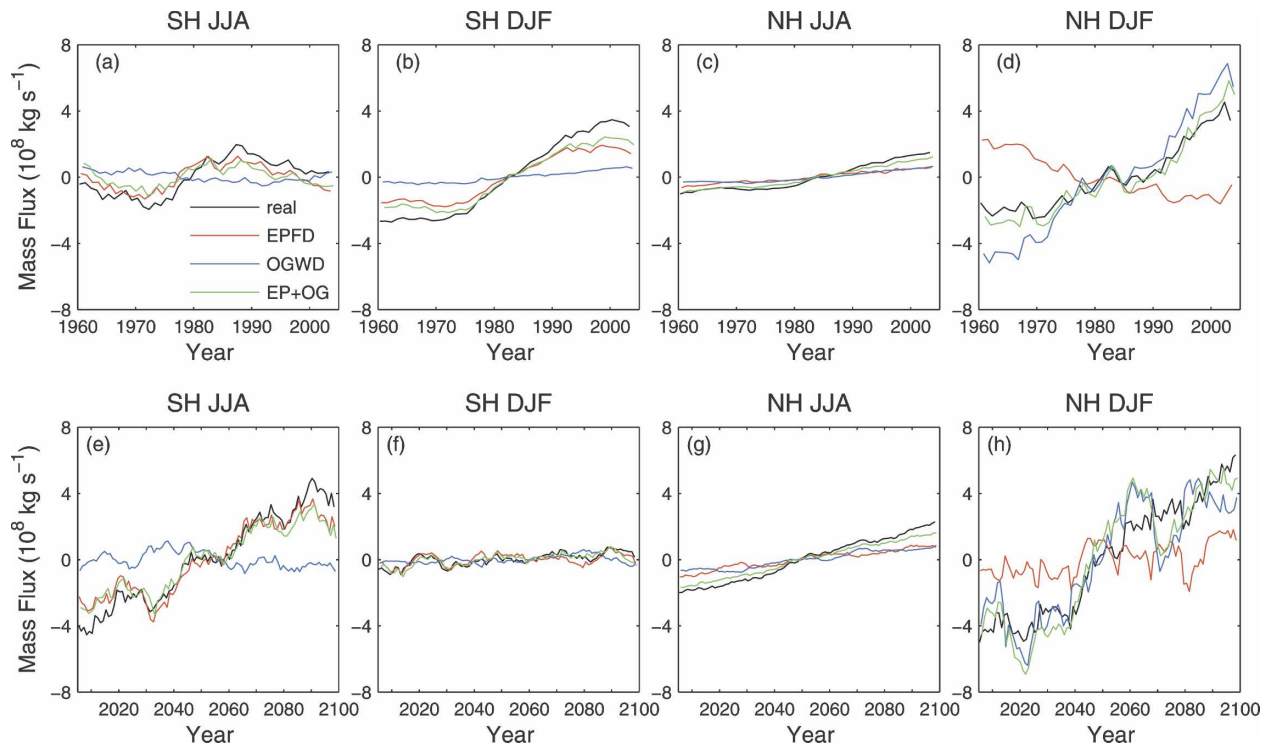
FIG. 7. Comparison of the changes of the NH and SH downward mass flux at 77 hPa for the (top) past and (bottom) future climate simulations. The black line is the "real" mass flux calculated from the residual streamfunction. The red and blue lines denote, respectively, change of mass flux resulting from planetary wave and orographic gravity wave forcing, which are calculated using the downward control principle. The green line indicates the total effects of planetary waves and orographic gravity waves (red line + blue line).
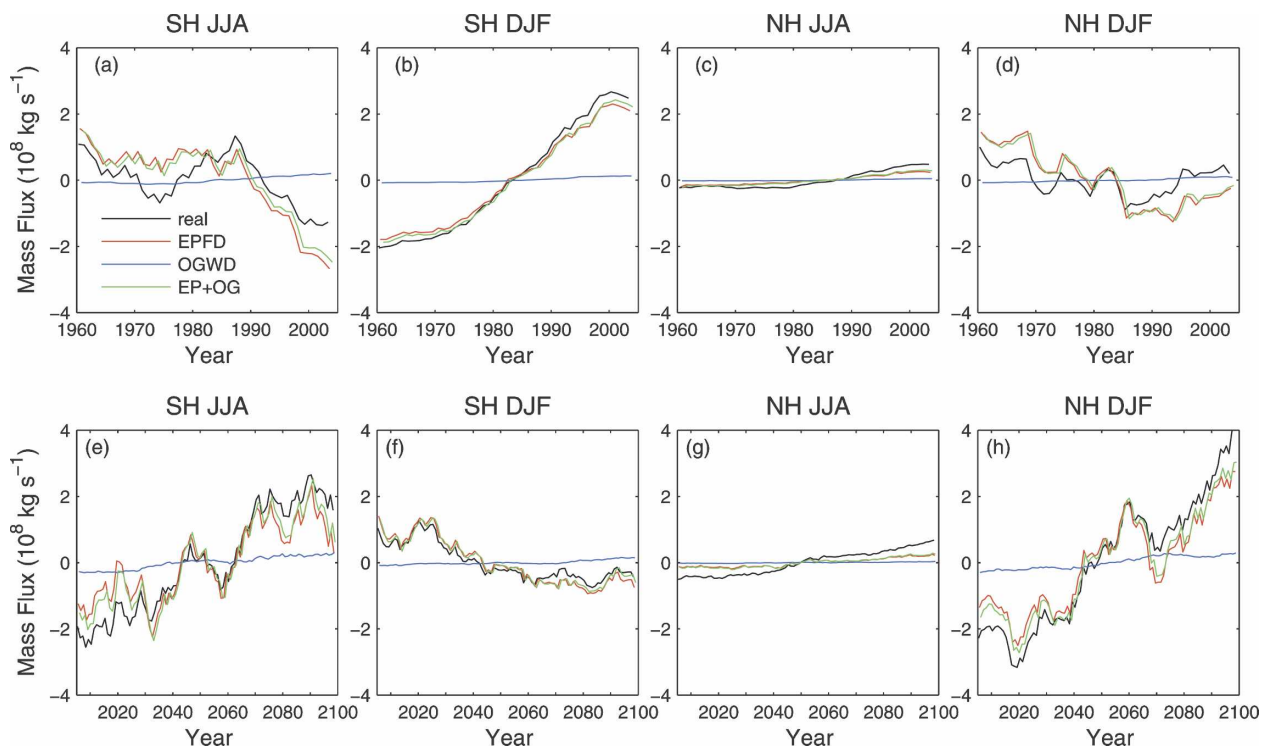

FIG. 8. Same as in Fig. 7, but for 46 hPa.

marily orographic gravity waves at 77 hPa to planetary waves at 46 hPa. In contrast to the future simulation, the NH winter planetary wave forcing in the past run had similar changes at 46 and 77 hPa (Figs. 7d and 8d), but the overall trend of the mass flux was opposite.

6. Change of planetary wave activity

An important question is why the SH planetary wave activity in the solstice seasons exhibited different trends between the past and future climate simulations. To answer this, the meridional temperature gradient in the SH extratropical UTLS region is investigated.

Planetary wave activity in the stratosphere is sensitive to the meridional temperature gradient in the UTLS region. Climate change resulting from the GHG increase and ozone depletion enhances the temperature gradient, and, by thermal wind balance, increases the vertical shear of the zonal wind, resulting in a westerly shift. This leads to a change of the refractive index, which influences the propagation of planetary waves. It should be noted that a stronger westerly wind decreases the refractive index, whereas an enhanced vertical shear increases the refractive index. Hence, an increasing meridional temperature gradient in the UTLS does not necessarily lead to stronger planetary wave activity in the stratosphere (Hu and Tung 2002). In the summer season, however, a westerly shift in the stratospheric easterly will enhance the upward wave propagation. Therefore, an increase in the meridional temperature gradient in the summer UTLS will enhance planetary wave activity in the stratosphere.

Figures 9a–c show the changes in temperature (T), zonal wind (u), and EPFD in DJF for the 1960–2004 period. The changes were calculated from a linear regression of the seasonal mean data against time. In general, the temperature trend, with warmer troposphere and colder stratosphere, is consistent with previous studies of global warming (e.g., Rind et al. 1998). The largest temperature change was found in the Antarctic lower stratosphere, which is characterized by a strong cooling centered at ~150 hPa coupled with a warming at about 20 hPa (Fig. 9a). The warming is due to adiabatic heating from enhanced descending motion in the Antarctic stratosphere (Fig. 3). The cooling in the Antarctic lower stratosphere is attributed to ozone depletion in the past decades (section 7). The corresponding zonal wind change obeys the thermal wind balance (Fig. 9b). The Antarctic cooling and the tropical warming enhanced the latitudinal temperature gradient, leading to a westerly increase of the zonal wind from the troposphere through the lower stratosphere centered at ~60°S. The enhanced meridional temperature

gradient and the resulting westerly wind increase allowed greater planetary wave propagation into the stratosphere. The subsequent wave dissipation generated stronger easterly acceleration (Fig. 9c). Figures 9d,e show the change of the zonal wind acceleration from the divergence of the vertical and horizontal components of the EP flux. Here, $EPFD_z = (\partial F^z/\partial z)$ and $EPFD_y = (1/a \cos\phi)(\partial/\partial\phi)(F^\phi \cos\phi)$, where F^z and F^y are the vertical and horizontal components of the EP flux, respectively. Trends in $EPFD_z$ and $EPFD_y$ have opposite signs in the SH high-latitude stratosphere, but the net effect is to enhance the planetary wave forcing. Examining the corresponding changes of EP flux reveals that as more planetary wave activity propagated upward and penetrated more deeply into the stratosphere, more wave activity in the stratosphere was meridionally refracted toward the equator (not shown). The latter effect, however, was overwhelmed by the former one, resulting in stronger net planetary wave forcing. It should be noted that the simulated temperature and wind trends in the Antarctic lower stratosphere are larger than observed because of model ozone trend bias (section 7). Hence, the increase of the planetary wave forcing in the Antarctic stratosphere is likely to be smaller in the real atmosphere.

We should emphasize that it is the EPFD trend at the turnaround latitude that determines the planetary wave contribution to the trend of the total SH downwelling [(1)]. Figure 9c shows increased EPFD throughout most of the SH stratosphere, including the DJF turnaround latitude located at 41°S. As a result, planetary waves made a significant contribution to the SH mass flux increase (Fig. 7b).

In the future runs, the tropospheric temperature continued to increase, and the warming extended higher into the lower stratosphere (Fig. 10a). The most significant difference from the past runs was found in the Antarctic lower stratosphere, where the cooling in the past was reversed due to recovery of the Antarctic ozone. As a result, the meridional temperature gradient decreased in the SH extratropical UTLS region. The reduced meridional temperature gradient reversed the trend in planetary wave activity throughout much of the SH stratosphere (Fig. 10c). At the turnaround latitude (41°S), the EPFD trend changed sign from the lower to middle stratosphere, resulting in a small net vertical integral (1). Therefore, the planetary wave contributions to the SH mass flux trend was small (Fig. 7f).

7. Temperature change in the Antarctic lower stratosphere

The above analyses have demonstrated that the changes of the Antarctic lower-stratospheric tempera-
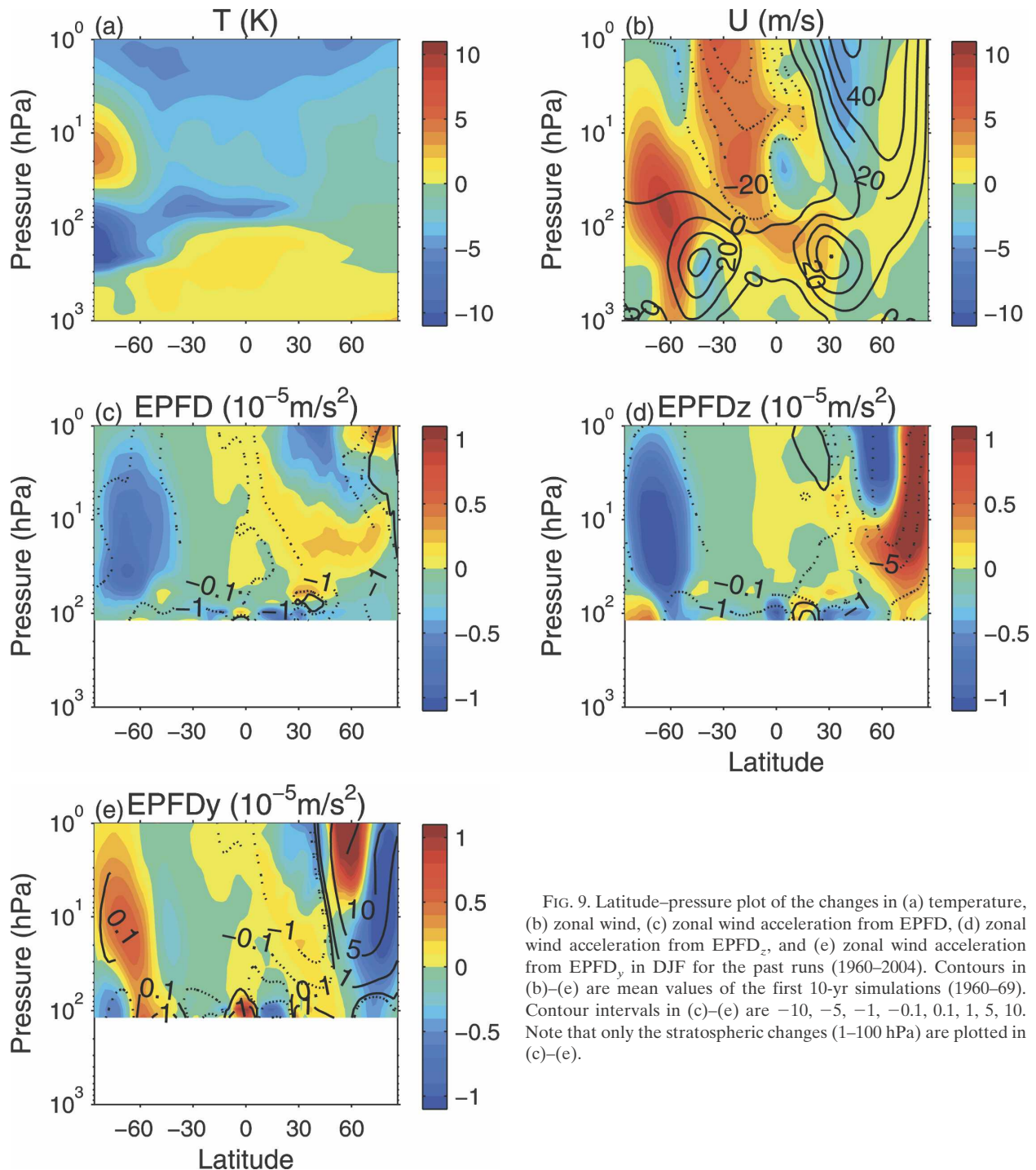
Fig. 9. Latitude–pressure plot of the changes in (a) temperature, (b) zonal wind, (c) zonal wind acceleration from EPFD, (d) zonal wind acceleration from EPFD$_z$, and (e) zonal wind acceleration from EPFD$_y$ in DJF for the past runs (1960–2004). Contours in (b)–(e) are mean values of the first 10-yr simulations (1960–69). Contour intervals in (c)–(e) are −10, −5, −1, −0.1, 0.1, 1, 5, 10. Note that only the stratospheric changes (1–100 hPa) are plotted in (c)–(e).

ture determined the trend in the planetary wave driving in the summer SH extratropics. In general, the polar stratospheric temperature is determined by both radiative and dynamical processes. However, radiative processes are dominant in driving the long-term variations of the Antarctic lower-stratospheric temperature during the SH spring and summer.

The evolution of the Antarctic lower-stratospheric temperature in the SH springtime is primarily a radiative response to the formation of the Antarctic ozone hole and its projected recovery (figure not shown). Figure 11 shows that variations in the Antarctic ozone and lower-stratospheric temperature are strongly correlated in the SH summer. This correlation largely is due to the
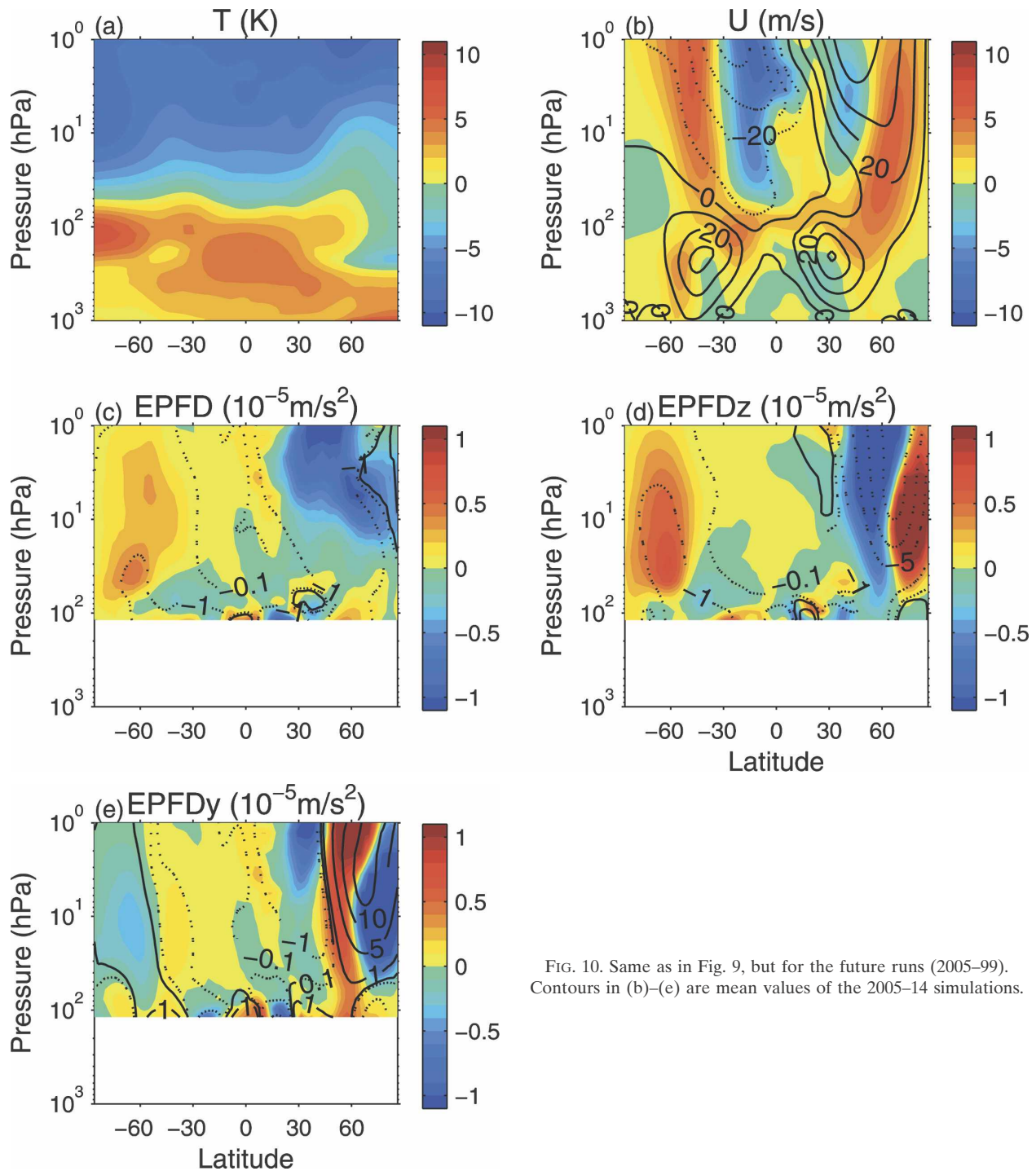
FIG. 10. Same as in Fig. 9, but for the future runs (2005–99). Contours in (b)–(e) are mean values of the 2005–14 simulations.

thermal memory of the lower stratosphere and the ozone photochemical memory (Thompson and Solomon 2002). Variations in summer Antarctic lower-stratospheric temperature and ozone are correlated with those in the late spring (Table 1). Note that not only the long-term trend, but the interannual variations

of ozone and lower-stratospheric temperature are strongly correlated as well (Table 1).

The cooling of the Antarctic lower stratosphere has been reported in many observational and modeling studies (e.g., Graf et al. 1998; Randel and Wu 1999; Rosier and Shine 2000). Using radiosonde, satellite,
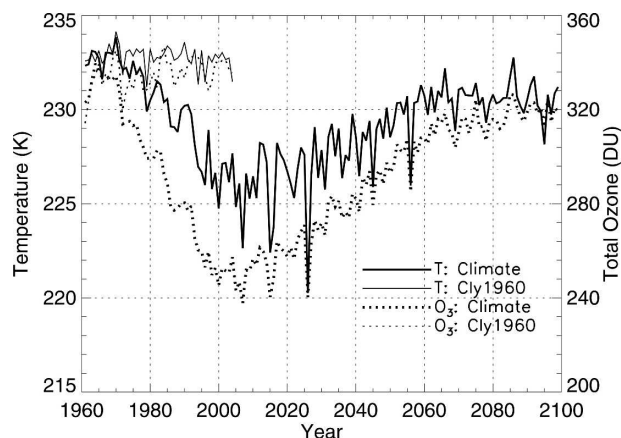
FIG. 11. Time sequences of the Antarctic (60°–90°S) DJF temperature at 120 hPa (solid line) and total ozone (dotted line). Thick lines are results of the past and future climate simulations. Data for the 1960–2004 and 2005–99 period are from the past and future runs, respectively. Thin lines are results of Cly1960.

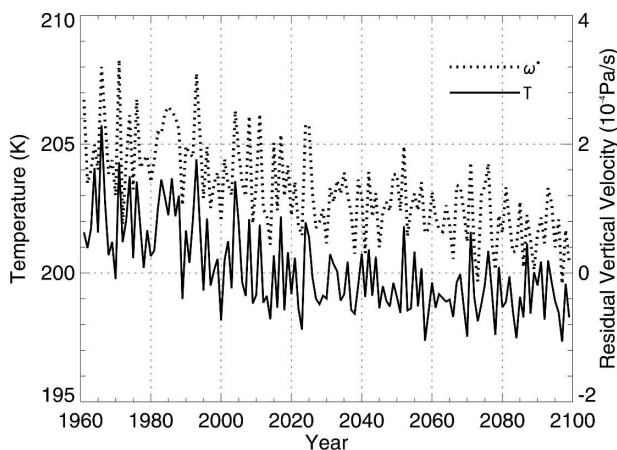FIG. 12. Time sequences of the Antarctic (60°–90°S) temperature at 120 hPa in August (solid line) and residual vertical velocity at 120 hPa in JJA (dotted line). Data for the 1960–2004 and 2005–99 period are from the past and future runs, respectively.

and reanalysis data, Randel and Wu (1999) showed that the sharp temperature decrease in the Antarctic lower stratosphere coincided with ozone depletion in the past 2 or 3 decades. The largest cooling occurred in the austral spring, but smaller temperature decreases extended into the summer. This cooling of the lower stratosphere was accompanied by significant warming at higher levels. Of interest is the cooling and warming pattern that descended with height from the austral spring to summer. Mahlman et al. (1994) investigated the impact of an ozone hole using a GCM. They found that the purely radiative effect of the ozone change would lead to a cooling throughout the Antarctic stratosphere and concluded that the upper stratosphere warming was due to increased adiabatic heating. Our past climate simulation results are consistent with these studies (Fig. 9a), including the descending of the cooling/warming structure (figure not shown). However, the model cooling is larger than observed, because the model has larger ozone trends than observed (Austin and Wilson 2006).

In contrast to summer, the winter polar lower-stratospheric temperature and the planetary wave activity are highly correlated (Newman et al. 2001). Figure 12 shows the time series of the area-weighted Antarctic temperature in August and the residual vertical velocity $(\overline{\omega}^*)$ in JJA. The August temperature is highly correlated with the JJA downwelling (correlation coefficient = 0.88), suggesting that the polar winter temperature change is controlled by dynamical processes.

In summary, we conclude that the intensification of the summer SH downward mass flux in the past decades was largely driven by ozone depletion during the same period. In the future climate simulation, the summer SH downward mass flux remained at about the same level as that of the early 2000s, consistent with predicted ozone recovery.

8. Experiment with fixed 1960 chlorine and bromine amounts

A more general question arises following the discussions in sections 6 and 7: what is the relative importance of ozone depletion versus other factors in driving the strengthening of the BDC? These other factors include GHG increase, the solar cycle, and volcanic eruptions. We addressed this issue by performing an experiment for the 1960–2004 period with fixed 1960 levels of chlorine and bromine concentrations.

Figure 13a compares the annually averaged global total ozone for the ensemble mean of the past runs (TRANS), the control run with fixed 1960 levels of halogen concentrations (Cly1960), and the time-slice run of fixed 1960 conditions (TS1960). The three time

TABLE 1. Correlation coefficients between the Antarctic total ozone and the Antarctic temperature at 120 hPa. The number in the parentheses is the coefficient after removal of the linear trend.

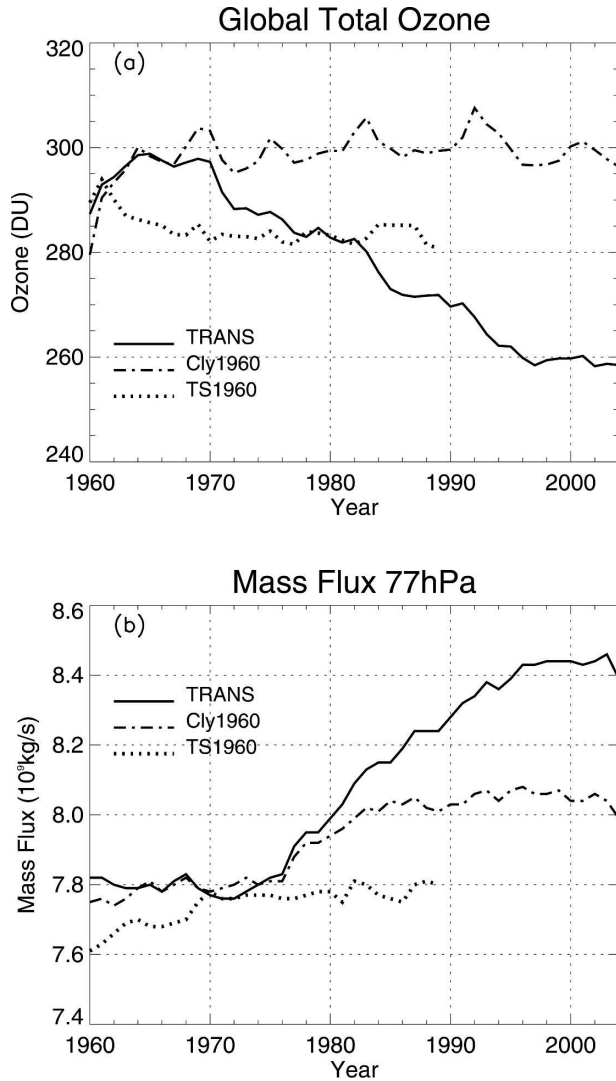|	1960–2004	
	DJF $T_{120 \text{ hPa}}$	Nov O_3
DJF O_3	0.96 (0.74)	0.98 (0.75)
Nov $T_{120 \text{ hPa}}$	0.92 (0.62)	0.95 (0.84)
	2005–2099	
	DJF $T_{120 \text{ hPa}}$	Nov O_3
DJF O_3	0.90 (0.88)	0.97 (0.81)
Nov $T_{120 \text{ hPa}}$	0.84 (0.72)	0.88 (0.96)

Global Total Ozone

Mass Flux 77hPa

FIG. 13. (a) Comparison of the annual mean global total ozone from the past climate simulations (TRANS), the time-slice simulation with 1960 conditions (TS1960), and the simulation with fixed 1960 halogen concentrations (Cly1960). (b) Comparison of the annual mean tropical upward mass flux at 77 hPa (11-yr running averaged) for the three experiments.

series are very different. Global total ozone in TRANS decreased by about 40 Dobson units (DUs) for the 1970–2000 period, while total ozone from Cly1960 oscillated around a level of 300 DU without a long-term trend. TS1960 total ozone reached an equilibrated state of about 280 DU after 1970. Figure 13a clearly shows that the increase of halogen concentrations in the atmosphere was responsible for the ozone depletion in the past 3 decades.

The TS1960 mass flux (Fig. 13b) reached approximately the same value as the other two experiments by about 1970 and remained at that level for the rest of the

run. This behavior confirms that the intensification of the BDC was driven by external factors. The increase of the 77-hPa upward mass flux started at about 1975 for the TRANS and Cly1960 simulations. The overall change of mass flux after 1975, which is defined as the difference between the 1995–2004 and 1965–74 mean, for TRANS and Cly1960, was 6.6×10^8 and 2.6×10^8 kg s^{-1}, respectively. The only difference in external forcing between the two simulations is due to ozone depletion, and so it is concluded that in the model, ozone depletion in the past accounted for 4×10^8 kg s^{-1} (60%) of the total increase of the tropical upward mass flux at 77 hPa.

Figure 11 shows that no Antarctic ozone hole formed in the Cly1960 simulation and that the Antarctic lower-stratospheric temperature did not have a cooling trend in the past. As a result, the increase of the latitudinal temperature gradient, and hence the planetary wave forcing, in the summer SH UTLS region was much weaker in Cly1960 than in TRANS (figure not shown). The increase of the SH downward mass flux at 77 hPa in DJF for the 1960–2004 period from Cly1960 (2.2×10^8 kg s^{-1}) was only 37% of that from TRANS (5.9×10^8 kg s^{-1}), similar to the annual average figures.

9. Change of orographic gravity wave forcing

As discussed in section 5, the mechanism for driving the increase of the downward mass flux in the lower stratosphere is different between the NH and SH. In both the past and future climate simulations, the largest increase of the NH downward mass flux occurred in DJF, which was due to an enhancement of the orographic gravity wave forcing (Fig. 7).

Although most general circulation models include an orographic gravity wave drag parameterization, there have been few reports of the change of orographic gravity wave forcing in a changing climate and its impact on the BDC. This is somewhat surprising, because orographic gravity waves tend to break in the UTLS region and the resulting wave drag is related to wind speed and static stability in that region. Therefore, the orographic gravity wave forcing in the lower stratosphere should be sensitive to climate change and should, in turn, alter the strength of the BDC.

Orographic gravity wave drag in AMTRAC is parameterized following Pierrehumbert (1986) and Stern and Pierrehumbert (1988). Although the details of this parameterization are different from other schemes, the principle is very similar. The wave drag (in the model layers) is calculated from a vertical profile of the wave momentum flux (at the interfaces of the model layers), which is determined by a base source flux and a vertical

profile of saturation flux. The source momentum flux at the surface is related to the near-surface wind speed and static stability, and the subgrid-scale orographic variance. The value of the saturation momentum threshold τ^* is given by

$$\tau^*(z) = -\rho(z)U^2(z)D/L \propto -\rho\,\frac{U^3(z)}{N(z)}, \qquad (2)$$

where ρ is the density, U is the wind speed, L is an effective horizontal mountain wavelength of 100 km, D is the gravity wave vertical wavelength, and N is the Brunt–Väisälä frequency. Here, D is calculated from the Wentzel–Kramers–Brillouin (WKB) theory, but can be approximated as (U/N) if the vertical shear term is omitted. The wave flux at a given altitude is equal to either the saturation threshold at that level (a process called gravity wave saturation), or the flux at the level immediately below, whichever is smaller. If the wave saturation threshold is achieved at the top interface of a model layer, the flux difference between the top and bottom interfaces is deposited at that layer. For example, wave drag at 77 hPa is calculated as the wave flux difference between 68 and 86 hPa, which are the top and bottom interfaces, respectively, of the 77-hPa layer.

According to the downward control principle, the residual vertical velocity (or the residual streamfunction) at a given altitude is determined by the vertically integrated wave forcing above that altitude. Provided that no momentum flux escapes through the top of the model and the integration is performed for a fixed latitude, the downward integration of wave drag from the model top to a given level is equivalent to the wave flux passing through that level. That is to say, under these assumptions, the gravity wave contribution to the mass flux at 77 hPa is equal to the gravity wave momentum flux at 86 hPa. The orographic gravity wave parameterization in AMTRAC allows flux to escape at the model top, but the impact of this flux leakage on the downward wave drag integral in the lower stratosphere is small, because the flux escaping through the model top is two orders of magnitude smaller than that in the lower stratosphere. The assumption that the integral in (1) can be performed for a fixed latitude approximately holds because surfaces of constant absolute angular momentum are very nearly vertically oriented. Therefore, by investigating the changes of the gravity wave momentum flux at 86 hPa, we can understand why the gravity wave contribution to mass flux at 77 hPa has increased in the NH winter season.

The evolution of the orographic gravity wave momentum flux at 86 hPa during the NH winter season at

27°N is shown in Fig. 14a. Note that the NH turnaround latitude in DJF was located at about 27°N; hence, the increase of wave momentum flux shown in Fig. 14a approximately reflects the changes of the NH downward mass flux shown in Figs. 7d,h.

There are two possible mechanisms for the wave flux increase at 86 hPa—it maybe be due to an increase in the source flux and/or an increase in the saturation flux threshold at 86 hPa, such that increased wave flux passes through 86 hPa. Figure 14a shows that while the wave source significantly strengthened in the 1960–80 period, there was no further increase after 1980. In contrast, the wave flux at 86 hPa had an upward trend from the middle 1960s to the late 2080s. Therefore, we conclude that the increase of wave flux at 86 hPa is not due to a strengthening of the wave source, at least for the 1980–2080 period.

According to (2), an increase in wind speed and/or a decrease in static stability would increase the saturation wave momentum threshold. Figure 14b shows that both factors contributed to the increase of the saturation threshold at 86 hPa, but the increase of the wind speed was the dominant factor because it has a larger trend and the saturation flux is proportional to the cube of the wind speed. The wind speed exhibited a nearly uniform increase of 33% for the 1960–2100 period. The Brunt–Väisälä period increased by about 8% in the past simulation and by about 4% in the future simulation. The increase in the wind speed in the NH midlatitude lower stratosphere was attributed to an enhanced meridional temperature gradient, which was due to a warming in the low-latitude UTLS and a cooling in the Arctic lower stratosphere (Figs. 9a and 10a). The decrease in the static stability in the lower stratosphere in the past simulation was caused by the warming of the troposphere and the cooling of the stratosphere resulting from the GHG increase and ozone depletion. In the future simulation, the warming extended upward into the lower stratosphere. As a result, the decrease of the static stability was weaker in the future runs than in the past runs.

Increases in the wave saturation threshold lead to decreased filtering of wave flux. To understand better how this mechanism works, changes in the wave flux carried by saturated and unsaturated waves are examined. At a given time and location (longitude, latitude, and level), wave flux is either unsaturated (i.e., smaller than the local saturation threshold) or saturated (i.e., constrained by the local saturation threshold). Hence, orographic gravity waves can be partitioned into the following two groups: unsaturated and saturated waves. Figure 14a shows the evolution of the zonally integrated (i.e., longitudinal sum) flux associated with un-
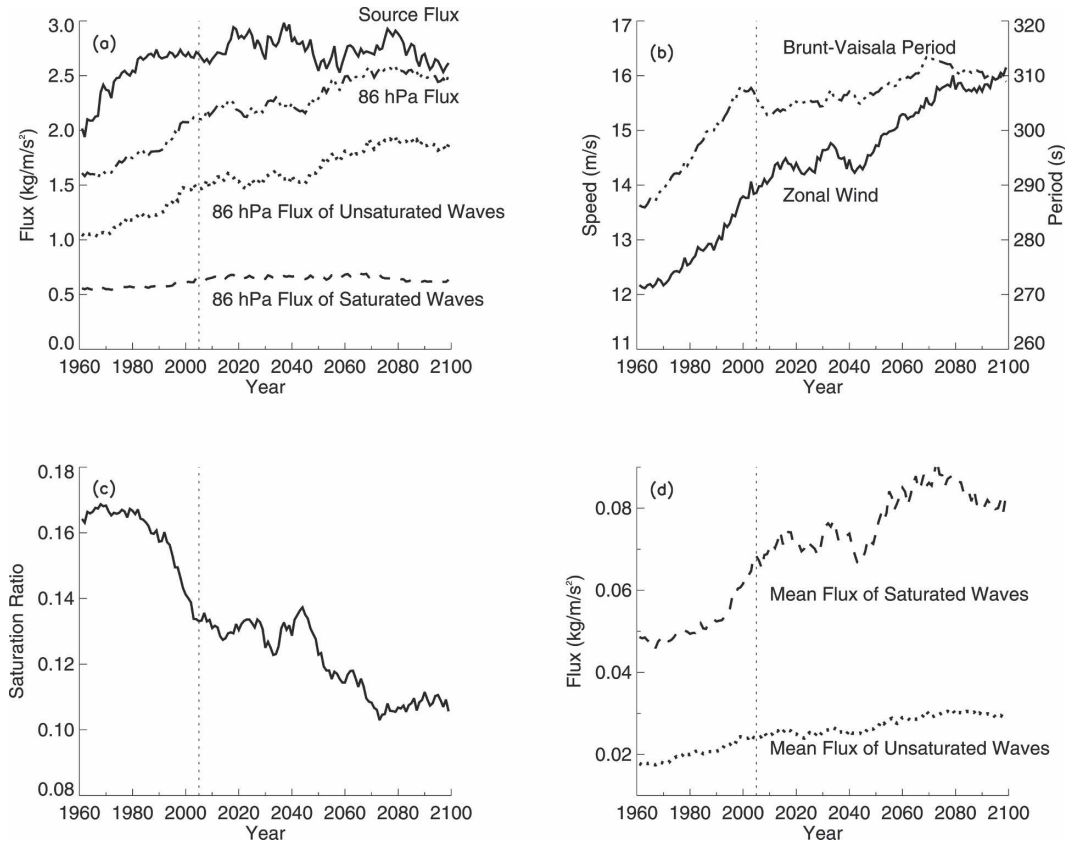
FIG. 14. Diagnostics of the orographic gravity wave parameterization at 27°N and 86 hPa in DJF. All results are daily averaged values for DJF. The vertical dotted line in year 2005 in all panels indicates that data for the 1960–2004 and 2005–99 period are from the past and future runs, respectively. (a) The zonally integrated orographic gravity wave source flux (solid), the zonally integrated flux of all waves (dash–dot), and unsaturated (dotted) and saturated waves (dashed) are shown. Note that the dash–dot curve is the sum of the dotted and dashed curves. For clarity, the curve representing source flux has been offset downward by 2.8 kg m s^{-2}. (b) The zonal mean zonal wind speed (solid) and Brunt–Väisälä period (dash–dot); (c) the saturation ratio, which is defined as the ratio of the number of longitude grids at which the wave flux is saturated to the number of longitude grids at which the wave flux is either saturated or unsaturated; and (d) the zonally normalized flux of unsaturated (dotted) and saturated (dashed) waves are shown. The normalization is calculated by dividing the zonally integrated flux of saturated and unsaturated waves shown in (a) with the number of longitudinal grids at which the fluxes are saturated and unsaturated, respectively.

saturated and saturated waves at 27°N and 86 hPa. Interestingly, the trend in the total wave flux is almost solely due to an increase in the flux of unsaturated waves, while the flux associated with saturated waves remained almost unchanged. The increase in the flux of unsaturated waves is because some previously saturated waves became unsaturated because of the increased saturation threshold. As the saturation threshold increases, more and more wave fluxes are not constrained by the saturation threshold. Therefore, the saturation ratio (defined as the ratio of the number of longitude grids at 27°N at which the wave flux is saturated to the number of longitude grids at which the wave flux is either saturated or unsaturated) will decrease. Figure 14c shows that the saturation ratio at

86 hPa significantly decreased during the course of the simulations, indicating that less wave flux was filtered out below 86 hPa and more wave flux passed through 86 hPa. Figure 14d shows that the mean flux of saturated and unsaturated waves also increased in the simulations. Here the mean flux is the zonally normalized flux, which is obtained by dividing the zonally integrated flux shown in Fig. 14a with the number of longitudinal grids at which the wave fluxes are saturated and unsaturated, respectively. The increase in the mean flux of saturated waves is a direct consequence of the increased saturation threshold. However, the increase in the mean flux of saturated waves is compensated by the decrease in the saturation ratio, resulting in a nearly unchanged zonally integrated flux of saturated waves.

10. Conclusions

The GFDL coupled chemistry–climate model simulated an intensification of the Brewer–Dobson circulation throughout the lower-to-middle stratosphere in the past (1960–2004) and future (2005–2100) simulations. A downward control analysis revealed that both resolved planetary waves and parameterized orographic gravity waves contributed to the increase of the BDC. The relative importance of the two types of wave forcing was dependent on the location and the season. In the lower stratosphere at 77 hPa, the change of the SH downward mass flux was primarily determined by the planetary wave activity, whereas the increase of the NH downward mass flux was mainly driven by the orographic gravity wave drag.

The intensification of the BDC exhibited a strong seasonal structure in the past runs, with DJF accounting for about 40% of the annual increase of the tropical upward mass flux. In the future runs, the increase of BDC was nearly uniformly distributed in the four seasons. It is found that this different seasonality was largely caused by the SH downward mass flux trend and was closely related to the Antarctic ozone depletion in the past decades and its projected recovery in the future.

In the summer SH during the past 2–3 decades, the Antarctic ozone depletion acted to increase the stratospheric planetary wave activity by enhancing the meridional temperature gradient through cooling the Antarctic lower stratosphere. The enhanced temperature gradient and the resulting westerly shift of the zonal wind increased planetary wave activity in the stratosphere. This led to an increased downward mass flux. In contrast, in the future simulation, with the recovery of the Antarctic ozone and the associated warming of the summer Antarctic lower stratosphere, the meridional temperature gradient in the Antarctic lower stratosphere was reduced, leading to a slight decrease of the stratospheric planetary wave forcing. As a result, the SH summer downward mass flux did not increase in the future climate simulation.

Previous modeling studies have shown that the BDC will intensify due to both greenhouse gas increase and ozone depletion, but there are no quantitative analyses of the relative importance of the two factors in the literature, as far as we know. In an attempt to separate the impact of ozone depletion on the BDC, an experiment was carried out with fixed chlorine and bromine amounts at 1960 levels. The results show that about 60% of the increase in the lower-stratospheric upward mass flux in the past climate is caused by ozone depletion, while the remaining 40% of the increase is attrib-

uted to greenhouse gas increase, the solar cycle, and volcanic aerosols. The dominance of the ozone impact is because, for the case of the SH summer downward mass flux, ozone depletion produced a much stronger temperature change in the lower stratosphere than other factors did. It should be noted that AMTRAC simulated a larger ozone depletion trend than that observed in the 1980–99 period (Austin and Wilson 2006). Therefore, the impact of the ozone depletion is likely to be smaller in the real atmosphere than that suggested by the model results.

Temperature and wind changes in the UTLS region not only influence planetary wave propagation, but also affect orographic gravity wave drag. The orographic gravity wave drag and its change are strongest in the NH winter. It was found that the increase of the orographic gravity wave forcing was not caused by strengthening of the wave source, but by an increase in the wave saturation threshold in the lower stratosphere, which led to decreased filtering of wave flux below 77 hPa and greater wave flux deposition above 77 hPa. Both an increase in the zonal wind speed and a decrease in the static stability contributed to the increase in the wave saturation threshold, but the wind effect was more prominent because the saturation threshold is proportional to the cube of the wind speed and the wind speed had a stronger trend than the static stability. The increase in the wind speed in the NH winter was caused by the enhanced meridional temperature gradient. The decrease in the static stability in the lower stratosphere was a direct consequence of troposphere warming and stratosphere cooling resulting from the GHG increase and/or ozone depletion.

The intensification of the BDC in the lower stratosphere was reduced in the future simulation compared with the past simulation, in part due to ozone recovery. Other forcing factors, most importantly SSTs, could also have had an impact. Observed SSTs were used for the past runs, while SSTs from a coupled atmosphere–ocean model simulation were taken for the future runs. How these different SST datasets influence the evolution of the BDC is unclear. We compared the tropical upwelling in the 15-yr overlap period of 1990–2004 between the past and future simulations and found no systematic difference (figure not shown). However, 15-yr trends in upwelling are too uncertain to provide reliable information and new simulations will be needed to distinguish the SST impacts from other factors.

REFERENCES

Alexander, M. J., and T. J. Dunkerton, 1999: A spectral parameterization of mean flow forcing due to breaking gravity waves. *J. Atmos. Sci.,* **56,** 4167–4182.

Austin, J., and N. Butchart, 2003: Coupled chemistry-climate model simulations for the period 1980 to 2020: Ozone depletion and the start of ozone recovery. *Quart. J. Roy. Meteor. Soc.,* **129,** 3225–3249.

——, and R. J. Wilson, 2006: Ensemble simulations of the decline and recovery of stratospheric ozone. *J. Geophys. Res.,* **111,** D16314, doi:10.1029/2005JD006907.

——, J. Wilson, F. Li, and H. Vömel, 2007: Evolution of water vapor concentrations and stratospheric age of air in coupled chemistry-climate model simulations. *J. Atmos. Sci.,* **64,** 905–921.

Butchart, N., and A. A. Scaife, 2001: Removal of chlorofluorocarbons by increased mass exchange between the stratosphere and troposphere in a changing climate. *Nature,* **410,** 799–802.

——, and Coauthors, 2006: Simulations of anthropogenic change in the strength of the Brewer-Dobson circulation. *Climate Dyn.,* **27,** 727–741.

Delworth, T. L., and Coauthors, 2006: GFDL's CM2 global coupled climate models. Part I: Formulation and simulation characteristics. *J. Climate,* **19,** 643–674.

Eichelberger, S. J., and D. L. Hartmann, 2005: Changes in the strength of the Brewer-Dobson circulation in a simple AGCM. *Geophys. Res. Lett.,* **32,** L15807, doi:10.1029/2005GL022924.

GFDL Global Atmospheric Model Development Team, 2004: The new GFDL global atmosphere and land model AM2–LM2: Evaluation with prescribed SST simulations. *J. Climate,* **17,** 4641–4673.

Graf, H.-F., I. Kirchner, and J. Perlwitz, 1998: Changing lower stratosphere circulation: The role of ozone and greenhouse gases. *J. Geophys. Res.,* **103,** 11 251–11 261.

Haynes, P. H., C. J. Marks, M. E. McIntyre, T. G. Shepherd, and K. P. Shine, 1991: On the "downward control" of extratropical diabatic circulations by eddy-induced mean zonal flow. *J. Atmos. Sci.,* **48,** 651–678.

Holton, J. R., 1995: Stratosphere-troposphere exchange. *Rev. Geophys.,* **33,** 403–439.

Houghton, J. T., X. Ding, D. J. Griggs, M. Noguer, P. J. van der Linden, X. Dai, K. Maskell, and C. A. Johnson, Eds., 2001: *Climate Change 2001: The Scientific Basis.* Cambridge University Press, 881 pp.

Hu, Y., and K. K. Tung, 2002: Interannual and decadal variations of planetary wave activity, stratosphere cooling, and Northern Hemisphere annual mode. *J. Climate,* **15,** 1659–1673.

Mahlman, J. D., J. P. Pinto, and L. J. Umscheid, 1994: Transport, radiative, and dynamical effects of the Antarctic ozone hole: A GFDL "SKYHI" model experiment. *J. Atmos. Sci.,* **51,** 489–508.

Newman, P. A., E. R. Nash, and J. E. Rosenfield, 2001: What controls the temperature of the Arctic stratosphere during the spring? *J. Geophys. Res.,* **106,** 19 999–20 010.

Pierrehumbert, R. T., 1986: An essay on the parameterization of orographic gravity wave drag. *Proc. Seminar/Workshop on Observation, Theory and Modeling of Orographic Effects,* Vol. 1, Reading, United Kingdom, ECMWF, 251–282.

Randel, W. J., and F. Wu, 1999: Cooling of the Arctic and Antarctic polar stratospheres due to ozone depletion. *J. Climate,* **12,** 1467–1479.

Rind, D., D. Shindell, P. Lonergan, and N. K. Balachandran, 1998: Climate change and the middle atmosphere. Part III: The double CO_2 climate revisited. *J. Climate,* **11,** 876–894.

Rosenlof, H. K., 1995: Seasonal cycle of the residual mean meridional circulation in the stratosphere. *J. Geophys. Res.,* **100,** 5173–5191.

Rosier, S. M., and K. P. Shine, 2000: The effect of two decades of ozone change on stratospheric temperature as indicated by a general circulation model. *Geophys. Res. Lett.,* **27,** 2617–2620.

Shindell, D. T., S. Wong, and D. Rind, 1997: Interannual variability of the Antarctic ozone hole in a GCM. Part I: The influence of tropospheric wave variability. *J. Atmos. Sci.,* **54,** 2308–2319.

Sigmond, M., P. C. Siegmund, E. Manzini, and H. Kelder, 2004: A simulation of the separate climate effects of middle-atmospheric and tropospheric CO_2 doubling. *J. Climate,* **17,** 2352–2367.

Stern, W. F., and R. T. Pierrehumbert, 1988: The impact of an orographic gravity wave drag parameterization on extended range predictions with a GCM. Preprints, *Eighth Conf. on Numerical Weather Prediction,* Baltimore, MD, Amer. Meteor. Soc., 745–750.

Thompson, D. W. J., and S. Solomon, 2002: Interpretation of recent Southern Hemisphere climate change. *Science,* **296,** 895–899.

WMO, 2002: Scientific assessment of ozone depletion: 2002. NOAA/NASA/UNEP/EC WMO Global Ozone Research and Monitoring Project Rep. 47, 498 pp.